

Detection of jet launching structure near the supermassive black hole in M87

Authors: **Sheperd S. Doeleman^{1*}, Vincent L. Fish¹, David E. Schenck^{1,2†}, Christopher Beaudoin¹, Ray Blundell³, Geoffrey C. Bower⁴, Avery E. Broderick⁵, Richard Chamberlin⁶, Robert Freund², Per Friberg⁷, Mark A. Gurwell³, Paul T. P. Ho⁸, Mareki Honma⁹, Makoto Inoue⁸, Thomas P. Krichbaum¹⁰, James Lamb¹¹, Abraham Loeb³, Colin Lonsdale¹, Daniel P. Marrone², James M. Moran³, Tomoaki Oyama⁹, Richard Plambeck⁴, Rurik A. Primiani³, Alan E. E. Rogers¹, Daniel L. Smythe¹, Jason SooHoo¹, Peter Strittmatter², Remo P. J. Tilanus^{7,12}, Michael Titus¹, Jonathan Weintroub³, Melvyn Wright⁴, Ken H. Young³, Lucy Ziurys²**

Affiliations:

¹MIT Haystack Observatory, Off Route 40, Westford, MA 01886, USA.

²Arizona Radio Observatory, Steward Observatory, University of Arizona, 933 N. Cherry Ave., Tucson AZ 85721-0065, USA.

³Harvard Smithsonian Center for Astrophysics, 60 Garden Street, Cambridge, MA 02138, USA.

⁴UC Berkeley, Department of Astronomy, 601 Campbell, Berkeley CA 94720-3411 USA.

⁵Perimeter Institute, 31 Caroline St., N. Waterloo, Ontario, Canada N2L 2Y5.

⁶Caltech Submillimeter Observatory, 111 Nowelo St., Hilo, Hawai'i 96720, USA.

⁷James Clerk Maxwell Telescope, Joint Astronomy Centre, 660 N. A'ohoku Place University Park, Hilo, Hawaii 96720, U.S.A.

⁸Academia Sinica Institute for Astronomy and Astrophysics, 11F Astronomy-Mathematics Bldg., National Taiwan University, No. 1, Roosevelt Rd., Sec. 4 Taipei 10617, Taiwan R.O.C.

⁹National Astronomical Observatory of Japan, 2-21-1 Osawa, Mitaka, Tokyo 181-8588 Japan

¹⁰Max-Planck-Institut für Radioastronomie, Auf dem Hügel 69, 53121 Bonn, Germany.

¹¹OVRO, California Institute of Technology, 100 Leighton Lane, Big Pine, CA 93513-0968 U.S.A.

¹²Netherlands Organization for Scientific Research, Laan van Nieuw Oost-Indie 300, NL2509 AC The Hague, The Netherlands.

†Current address: University of Colorado at Boulder, Dept. of Astrophysical and Planetary Sciences, 391 UCB, Boulder, CO, 80309 USA.

*sdoeleman@haystack.mit.edu

Abstract: Approximately 10% of active galactic nuclei (AGN) exhibit relativistic jets, which are powered by accretion of matter onto super massive black holes. While the measured width profiles of such jets on large scales agree with theories of magnetic collimation, predicted structure on accretion disk scales at the jet launch point has never been detected. We report radio interferometry measurements at 1.3mm wavelength of the elliptical galaxy M87 that spatially resolve the black hole accretion disk system at the jet base. The derived size of 4.9 ± 0.4 Schwarzschild radii is significantly smaller than the innermost edge of a retrograde accretion disk, and implies that the M87 jet is powered by an accretion disk in a prograde orbit around a spinning black hole.

One Sentence Summary: Black hole sized structure is detected at the base of a relativistic jet in the center of an active galaxy.

Main Text: The compact central regions of some galaxies are so luminous that they outshine the combined output of all other energy sources in the galaxy. The small size and high power output of these active galactic nuclei (AGN) are most plausibly explained by the conversion of gravitational energy through accretion onto a super massive black hole. Many AGN produce powerful collimated jets of relativistic particles that can extend for hundreds and thousands of light-years, providing an important mechanism for redistributing matter and energy on large scales that affect galactic evolution (1). Jets are thought to form through magnetic acceleration processes located within the accretion flow or at the central black hole itself (2-4), but no observations to date have had the angular resolution required to detect and confirm structure on these scales for extragalactic jet sources. High-resolution radio interferometry of these sources at cm wavelengths is limited by optical depth effects that obscure the innermost accretion region. For these reasons, it remains unclear if jet formation requires a spinning black hole (5,6), or if jets are likely to be launched from disks orbiting in the opposite direction (retrograde) of the spin of the black hole (7,8). To address these questions, we have assembled a Very Long Baseline Interferometry (VLBI) array operating at a wavelength of 1.3mm, where AGN become optically thin, and angular resolutions necessary to resolve the inner accretion disks of nearby AGN are obtained.

At a distance of $16_{-1.1}^{+1.3}$ Mpc (9) and with a mass most recently measured to be $(6.6 \pm 0.4) \times 10^9 M_{\odot}$ (10), the Schwarzschild radius of the M87 black hole ($R_{\text{SCH}} = 2GM/c^2 = (6.3 \pm 0.4) \times 10^4 \text{ parsec} = (2.0 \pm 0.12) \times 10^{15} \text{ cm}$) subtends an angle of 8.1 ± 0.8 micro arcseconds, presenting us with the best known opportunity for studying the formation of relativistic jets on scales commensurate with the black hole and accretion disk. Radiating via synchrotron emission, the relativistic jet from M87 extends for hundreds of kilo parsecs and terminates in extended lobes of emission as it slows and interacts with the intergalactic medium. Closer to the galaxy's core, on hundreds of parsec scales, the radio jet is remarkably well collimated with an opening angle of less than 5 degrees (11), and is also clearly seen in the optical, ultra-violet, and x-rays (12,13) where the emission is primarily confined to knots along the central 'spine' of the jet. VLBI observations at wavelengths ranging from 3.5mm to 20cm, show that within 10's of milli arcseconds of the core, the jet opening angle, delineated by edge brightening in the outflow, increases to greater than 40° (14-18). This wide opening angle is a signature of the launch point for a magnetohydrodynamically (MHD) powered jet that has not yet had time to collimate (2), and identifies the VLBI core as the most likely site of the central black hole.

We observed M87 over three consecutive days with a 1.3mm wavelength VLBI array consisting of four telescopes at three geographical locations: the James Clerk Maxwell Telescope (JCMT) on Mauna Kea in Hawaii, the Arizona Radio Observatory's Submillimeter Telescope (SMT) in Arizona, and two telescopes of the Combined Array for Research in Millimeter-wave Astronomy (CARMA, located ~60m apart) in California. On Mauna Kea, the JCMT partnered with the Submillimeter Array (SMA), which housed the Hydrogen maser atomic frequency standard and wideband VLBI recording systems; the SMT and CARMA were similarly equipped. These special-purpose systems allowed two frequency bands of 512 MHz to be sampled at 2-bit precision and recorded at an aggregate rate of 4 Gigabits/second. Data recorded at all sites were shipped to MIT Haystack Observatory for processing on the Mark4 VLBI correlator. Once correlated, data for each VLBI scan (typically 10 minutes) were corrected for coherence losses due to atmospheric turbulence and searched for detections using established algorithms tailored for high frequency observations (see SI). M87 was clearly detected each day on all VLBI baselines, and the interferometric data were then calibrated to flux density units (Figure 1; see SI for details).

Clear detections on the long baselines to Hawaii (CARMA-JCMT and SMT-JCMT) represent the highest angular resolution observations of M87 reported in any waveband, and when combined with the CARMA-SMT baseline data they provide a robust means to measure the size of the M87 core, which is unresolved with longer wavelength VLBI. The baseline between the two CARMA antennae corresponds to angular scales of ~4 arcseconds and is sensitive to extended and much larger scale jet structure; these data were thus used to refine calibration of the antennas, but were excluded from analysis of the core component. To extract a size for the core, we fit a two-parameter circular Gaussian model to the 1.3mm VLBI data, deriving a total flux density and full width half maximum (FWHM) size for each day of observations. Sizes and flux densities fit separately for each day are consistent with each other at the 3σ level, indicating no significant variation in the 1.3mm core structure over the three days of observation. Fits on a plot of correlated flux density vs. baseline length are shown in Figure 1. When data from all three days are combined, the weighted least-squares best-fit model for the compact component results in a flux density of 0.98 ± 0.04 Jy and a FWHM of 40 ± 1.8 micro arcseconds (3σ errors). Conversion to units of Schwarzschild radius yields a value of $4.9 \pm 0.4 R_{\text{SCH}}$ (1σ errors) where the errors are completely dominated by uncertainties in the distance to M87 and the black hole mass. We adopt the circular Gaussian size derived using data from all three days for subsequent discussion.

Our VLBI observations cannot be used to fix the absolute position of this Gaussian component. However, two separate lines of evidence imply that this ultra-compact 1.3mm emission is in immediate proximity to the central super massive black hole at the jet-launch point. First, the long history of VLBI observations of M87 at many wavelengths can be used to construct a jet width profile that begins $\sim 100 R_{\text{SCH}}$ from the core and extends to core-separations of more than $10^4 R_{\text{SCH}}$. Figure 2 shows this profile along with a power law fit to the data that matches the functional form and characteristics exhibited by General Relativistic MHD simulations (18-20) in which the jet opening angle widens as it nears the black hole. The best-fit power law intersects the size of the 1.3mm emission region at a core distance of only $1.25 R_{\text{SCH}}$. Since the angle of the M87 jet axis to our line of sight is estimated to be within the range $15^\circ - 25^\circ$ (21), the de-projected distance of this intersection point lies in the range $3 - 5 R_{\text{SCH}}$. A second method of locating the 1.3mm emission derives from observations of the position shift of the M87 core

as a function of wavelength. The core corresponds to the point in the jet where opacity due to synchrotron self-absorption approaches unity, and this $\tau \sim 1$ surface should shift towards the jet launch point with decreasing observing wavelength. Multi-wavelength astrometric VLBI observations confirm that over a wide range of frequency, the absolute position of the core moves asymptotically towards the central black hole with a $\nu^{-0.94}$ dependence (21). This relation also places the 1.3mm emission at an apparent distance of just $1.25 R_{\text{SCH}}$ from the black hole. Such strong evidence for associating the M87 core with the central black hole contrasts with the case of blazar sources, in which relativistic jets are closely aligned to our line of sight and the core becomes visible hundreds of thousands of Schwarzschild radii from the central engine (22). In M87, the favourable geometry of a misaligned jet and increased transparency of the synchrotron emission at mm wavelengths (23) allows us direct access to the innermost central engine with 1.3mm VLBI.

The most plausible mechanisms for powering extragalactic jets involve conversion of the black hole rotational energy through the Blandford-Znajek (BZ) process (3), whereby magnetic fields lines cross the black hole event horizon or become locked into co-rotation with the black hole ergosphere, and launch Poynting flux dominated outflows. The inner portion of the accretion disk is not only the source of the magnetic fields threading the black hole, but also launches a disk-wind via the Blandford-Payne (BP) mechanism (4), which serves to collimate the jet. This BZ/BP combination forms a spine/sheath morphology in which a high velocity and narrow central jet from the black hole is surrounded by a slower outflow originating from the inner disk (6,24). In the case of M87, our line of sight is sufficiently off axis that the dominant contribution to the 1.3mm VLBI emission is from the slower moving sheath, anchored within the accretion disk (21). Thus, the critical size scale associated with the jet footprint is the Innermost Stable Circular Orbit (ISCO) of the black hole, within which matter quickly plunges to the event horizon. Full General Relativistic Magnetohydrodynamic (GRMHD) simulations of coupled black hole and disk jets show that the jet base coincides with the ISCO over a wide range of black hole spin (Figure 2) (5,19,25).

Based on this understanding of the M87 jet, and taking the 1.3mm VLBI size as the ISCO diameter, we can estimate the black hole spin and determine whether the accretion disk orbits in a prograde or retrograde sense. This is because the intrinsic ISCO diameter (D_{ISCO}) is sensitively dependent on black hole spin, with a value of $D_{\text{ISCO}} = 6 R_{\text{SCH}}$ for a non-spinning (Schwarzschild) black hole ($a=0$), and ranging from $D_{\text{ISCO}} = 9 R_{\text{SCH}}$ to $D_{\text{ISCO}} = 1 R_{\text{SCH}}$ for retrograde and prograde orbits, respectively, around a maximally spinning (Kerr) black hole ($a=1$). Strong lensing effects due to the Kerr space-time metric near the rotating black hole magnify the apparent size of the ISCO, with the relationship between observed ISCO size and black hole spin shown in Figure 3 (26; see also SI). The measured 1.3mm VLBI size corresponds to a prograde ISCO around a black hole with spin $a > 0.4$. This result explicitly excludes the possibility of a retrograde ISCO orbit in the accretion flow since all such orbits would be larger than the core size derived here. The smallest possible retrograde ISCO orbit would present an apparent diameter of $7.35 R_{\text{SCH}}$, more than 6σ larger than the observed size. This result provides direct confirmation of generally accepted theories that the spin axes of the accretion disk and black hole will be brought into alignment through a combination of Lense-Thirring precession (27) and gradual angular momentum transfer from the orbiting disk (28). Recent work has proposed that some jets may be powered via retrograde disks (7), but the size derived here provides strong evidence against such a scenario for M87.

As the sensitivity and resolution of the 1.3mm VLBI array improves, modelling of the data can move beyond simple Gaussian distributions to physically motivated models that include accretion physics, relativistic beaming and full GR ray tracing. Recent modelling of the M87 jet on Schwarzschild radius scales indicates that in many cases emission from a counter-jet will illuminate the black hole from behind, creating a bright feature at the last photon orbit (23,29). The relatively dim region interior to this ring is known as the black hole ‘shadow’ or ‘silhouette’, and its dimensions are determined by black hole mass, spin and inclination of the spin axis (30). Over a wide range of spin and inclination, the last photon ring of emission has a diameter of $D_{\text{RING}} = 10.4 GM/c^2$, so that fitting for the ring size yields an estimate of the black hole mass (31). In fact, the presence of such a shadow feature is not ruled out by the 1.3mm VLBI data presented here, which can be well fitted by a hybrid model combining a circular Gaussian to represent jet emission launched from the ISCO with a uniform annular ring at the last photon orbit (Figure S4 in SI). Though the current VLBI array cannot be used to meaningfully constrain this more complex model, there are two distinguishing characteristics of this hybrid approach that can be readily tested with future mm and submm VLBI arrays. The first is a predicted null in correlated flux density near baseline lengths of $4.5 \times 10^9 \lambda$, and the second is a 180-degree flip in interferometric phase between VLBI baselines on either side of this null. Longer baselines to new VLBI stations will bridge this null, providing a means to test both the flux density and phase signatures of the last photon ring, as well as the possibility of using the ring diameter to weigh nearby supermassive black holes. It is increasingly clear that strong gravity effects can dominate observed AGN structure on the scales newly accessible with short wavelength VLBI.

Planned improvements to the (sub)mm VLBI Array, including addition of the phased Atacama Large Millimeter Array (ALMA), will soon double angular resolution and increase sensitivity by an order of magnitude, enabling detailed comparison between observations and GRMHD simulations of jet production. In addition to imaging the ‘shadow’ feature, future 0.8mm and 1.3mm VLBI observations can be scheduled to span the spin-dependent ISCO period, which ranges from 5 days ($a=1$) to 1 month ($a=0$) for the mass of the M87 black hole, to search for signatures of orbiting structures in the accretion flow that would be imprinted on the jet emission. We note that the consistency of the 1.3mm VLBI sizes presented here, spanning three days of observation, does not reflect dramatic structural changes in the jet that might be expected due to accretion disk inhomogeneity for a black hole spinning near the maximum rate. In general, this work signals that Earth-sized (sub)mm VLBI networks are now able to provide angular resolutions capable of linking observations of compact objects dominated by strong-field GR to outflows on the largest galactic scales.

References and Notes:

1. D. Richstone, *et al.* Dressler, A., *et al.*, Supermassive black holes and the evolution of galaxies, *Nature* **395**, A14-A19 (1998).
2. D. L Meier, S. Koide, Y. Uchida, Magnetohydrodynamic production of relativistic jets, *Science* **291**, 84-92 (2001).
3. R.D. Blandford, R. L. Znajek, Electromagnetic extraction of energy from Kerr black holes, *MNRAS* **179**, 433-456 (1977).
4. R. D. Blandford, D. G. Payne, Hydromagnetic flows from accretion discs and the production of radio jets, *MNRAS* **199**, 883-903 (1982).

5. J. –P. De Villiers, J. F. Hawley, J. H. Krolik, S. Hirose, Magnetically driven accretion in the Kerr metric. III. unbound outflows, *Astrophys. J.* **620**, 878-888 (2005).
6. J. McKinney, General relativistic magnetohydrodynamic simulations of the jet formation and large-scale propagation from black hole accretion systems, *MNRAS* **368**, 1561-1582 (2006).
7. D. Garofalo, D. A. Evans, R. M. Sambruna, The evolution of radio-loud active galactic nuclei as a function of black hole spin, *MNRAS* **406**, 975-986 (2010).
8. Tchekhovskoy, A., McKinney, J., Prograde and retrograde black holes: whose jet is more powerful?, *MNRAS in press*, [arXiv:1201.4385](https://arxiv.org/abs/1201.4385), (2012).
9. J. L. Tonry, *et al.*, The SBF survey of galaxy distances. IV. SBF magnitudes, colors, and distances, *Astrophys. J.* **546**, 681-693 (2001).
10. K. Gebhardt, *et al.*, The black hole mass in M87 from Gemini/NIFS adaptive optics observations, *Astrophys. J.* **729**, 119-131 (2011).
11. J. A. Biretta, F. Zhou, F. N. Owen, Detection of proper motions in the M87 jet, *Astrophys. J.* **447**, 582-596 (1995).
12. E. S. Perlman, J. A. Biretta, W. B. Sparks, F. D. Macchetto, J. P. Leahy, the optical-near-infrared spectrum of the M87 jet from hubble space telescope observations, *Astrophys. J.* **551**, 206-222 (2001).
13. H. L. Marshall, *et al.*, A high-resolution X-ray image of the jet in M87, *Astrophys. J.* **564**, 683-687 (2002).
14. W. Junor, J. A. Biretta, M. Livio, Formation of the radio jet in M87 at 100 Schwarzschild radii from the central black hole, *Nature* **401**, 891-892 (1999).
15. T. P. Krichbaum, *et al.*, Sub-milliarcsecond imaging of Sgr A* and M 87, *Journal of Physics Conf. Series* **54**, 328-334 (2006).
16. C. Ly, R. C. Walker, W. Junor, High-frequency VLBI imaging of the jet base of M87, *Astrophys. J.* **660**, 200-205 (2007).
17. Y. Y. Kovalev, M. L. Lister, D. C. Homan, K. I. Kellermann, The inner jet of the radio galaxy M87, *Astrophys. J.* **668**, L27-L30 (2007).
18. K. Asada, M. Nakamura, The structure of the M87 jet: a transition from parabolic to conical streamlines, *Astrophys. J.* **745**, L28 (2012).
19. J. C. McKinney, R. D. Blandford, Stability of relativistic jets from rotating, accreting black holes via fully three-dimensional magnetohydrodynamic simulations, *MNRAS* **394**, L126-L130 (2009).
20. J. Gracia, N. Vlahakis, I. Agudo, K. Tsinganos, S. V. Bogovalov, synthetic synchrotron emission maps from MHD models for the jet of M87, *Astrophys. J.* **695**, 503-510 (2009).
21. K. Hada, *et al.*, An origin of the radio jet in M87 at the location of the central black hole, *Nature* **477**, 185-187 (2011).
22. A. P. Marscher, *et al.*, The inner jet of an active galactic nucleus as revealed by a radio-to- γ -ray outburst, *Nature* **452**, 966-969 (2008).

23. A. E. Broderick, A. Loeb, Imaging the black hole silhouette of M87: implications for jet formation and Black Hole spin, *Astrophys. J.* **697**, 1164-1179 (2009).
24. P. E. Hardee, Stability properties of strongly magnetized spine-sheath relativistic jets, *Astrophys. J.* **664**, 26-46 (2007).
25. C. P. Fragile, Effective inner radius of tilted black hole accretion disks, *Astrophys. J.* **706**, L246-L250 (2009).
26. A. Broderick, A. Loeb, R. Narayan, The event horizon of Sagittarius A*, *Astrophys. J.* **701**, 1357, (2009).
27. J. M. Bardeen, J. A. Petterson, The lense-thirring effect and accretion disks around Kerr black holes, *Astrophys. J.* **195**, L65-L67 (1975).
28. Gammie, C., Shapiro, S. & McKinney, J., Black hole spin evolution, *Astrophys. J.*, **602**, 312-319, (2004).
29. J. Dexter, J. C. McKinney, E. Agol, The size of the jet launching region in M87, *MNRAS* **421**, 1571-1528 (2012).
30. H. Falcke, F. Melia, E. Agol, Viewing the shadow of the black hole at the Galactic center, *Astrophys. J.* **528**, L13-L16 (2000).
31. T. Johannsen, *et al.*, Masses of nearby supermassive black holes with Very Long Baseline Interferometry, **arXiv:1201.0758** (2012).
32. Biretta, J.A., Junor, W. & Livio, M., Evidence for initial jet formation by an accretion disk in the radio galaxy M87, *New Astronomy Reviews*, **46**, 239-245, (2002).
33. A. E. Broderick, R. Blandford, Covariant magnetoionic theory – I. Ray propagation, *MNRAS* **342**, 1280-1290 (2003).
34. A. E. Broderick, A. Loeb, Imaging optically-thin hotspots near the black hole horizon of Sgr A* at radio and near-infrared wavelengths, *MNRAS* **367**, 905-916 (2006).
35. V. L. Fish, *et al.*, 1.3 mm wavelength VLBI of Sagittarius A*: detection of time-variable emission on event horizon scales, *Astrophys. J.* **727**, L36 (2011).
36. S. S. Doeleman, *et al.*, Structure of Sagittarius A* at 86 GHz using VLBI closure quantities, *Astron. J.* **121**, 2610 (2001).
37. S. S. Doeleman, *et al.*, Event-horizon-scale structure in the supermassive black hole candidate at the Galactic Centre, *Nature* **455**, 78 (2008).
38. A. E. E. Rogers, S. S. Doeleman, J. M. Moran, Fringe detection methods for very long baseline arrays, *Astron. J.* **109**, 1391 (1995).
39. J. M. Bardeen, W. H. Press, S. A. Teukolsky, Rotating black holes: locally nonrotating frames, energy extraction, and scalar synchrotron radiation, *Astrophys. J.* **178**, 347 (1972).

Acknowledgments: High frequency VLBI work at MIT Haystack Observatory is supported by grants from the National Science Foundation. The Submillimeter Array is a joint project between the Smithsonian Astrophysical Observatory and the Academia Sinica Institute of Astronomy and Astrophysics. The Caltech Submillimeter Observatory is funded under the National Science Foundation grant AST-0838261. We thank Gregory Weaver for the loan of a frequency reference from John Hopkins University Applied Physics Labs; Irv Diegel, Robert Vessot, David Phillips and Edward Mattison for assistance with Hydrogen Masers; the NASA Geodesy Program for loan of the CARMA Hydrogen Maser; John Test, Paul Yamaguchi, George Reiland, Jim Hoge and Mark Hodges for technical assistance; and the staff at all participating facilities. We also thank William Junor and John Biretta for providing us with data used in this report.

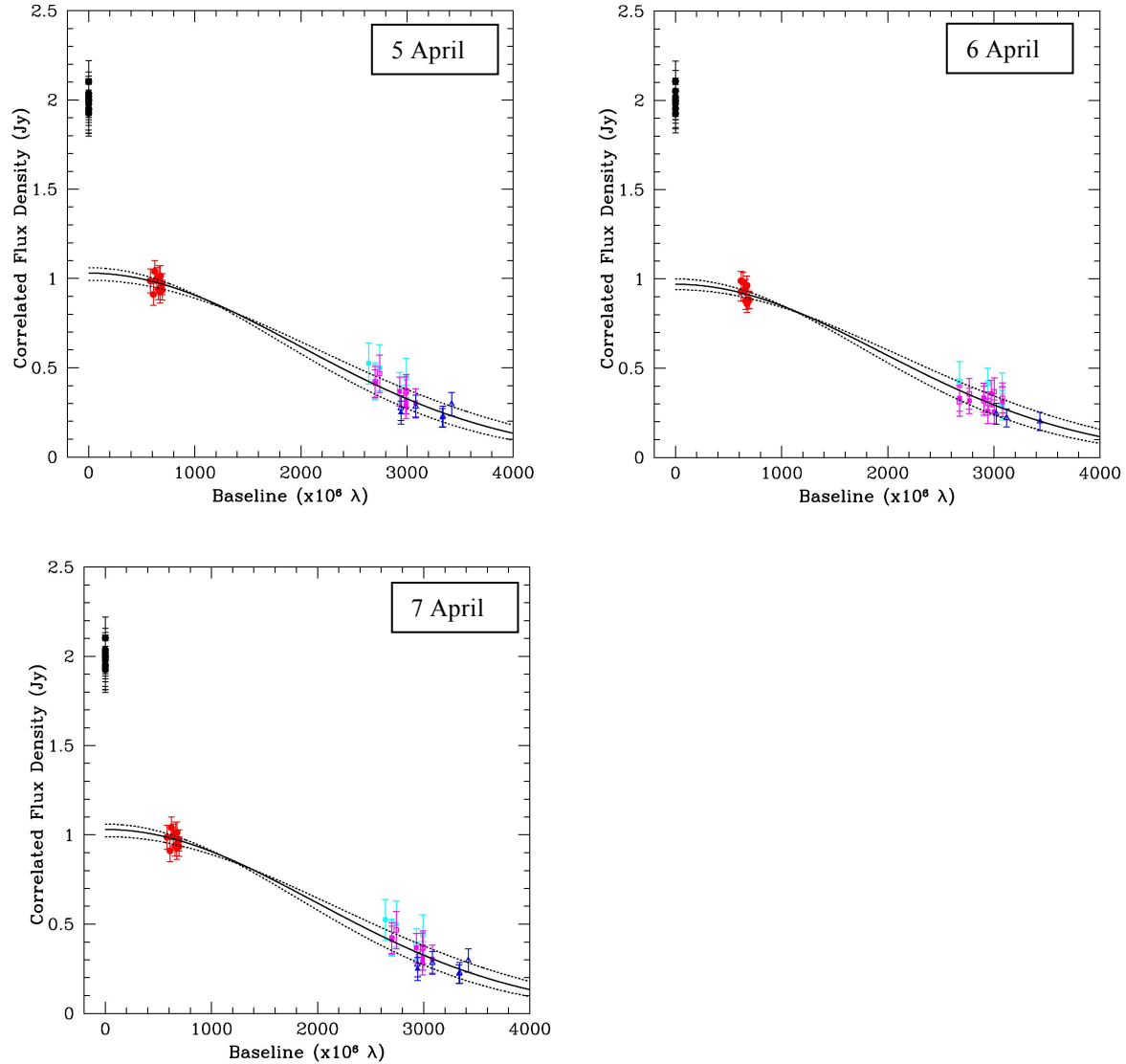


Fig. 1. Measuring the size of the M87 core with 1.3~mm VLBI. Plots of correlated flux density vs. baseline length for each of the three observing nights (2009 April 5, 6, 7 - left to right) are shown. Black points near zero-baseline length show flux density on the ~ 60 m baseline between the two CARMA dishes, which we measure to be 2.0 Jy. The CARMA-SMT baselines are shown in red; the two baselines from CARMA dishes to the JCMT are shown in magenta and teal; the SMT-JCMT baseline is shown in blue. Calibration errors of 5% have been added in quadrature to the 1σ random errors associated with the incoherent fringe search performed on each baseline. Solid black curves show the linear least squares best-fit circular Gaussian models (see Table 1 in SI). Dotted lines show the circular Gaussian models corresponding to the 3σ limits on source size.

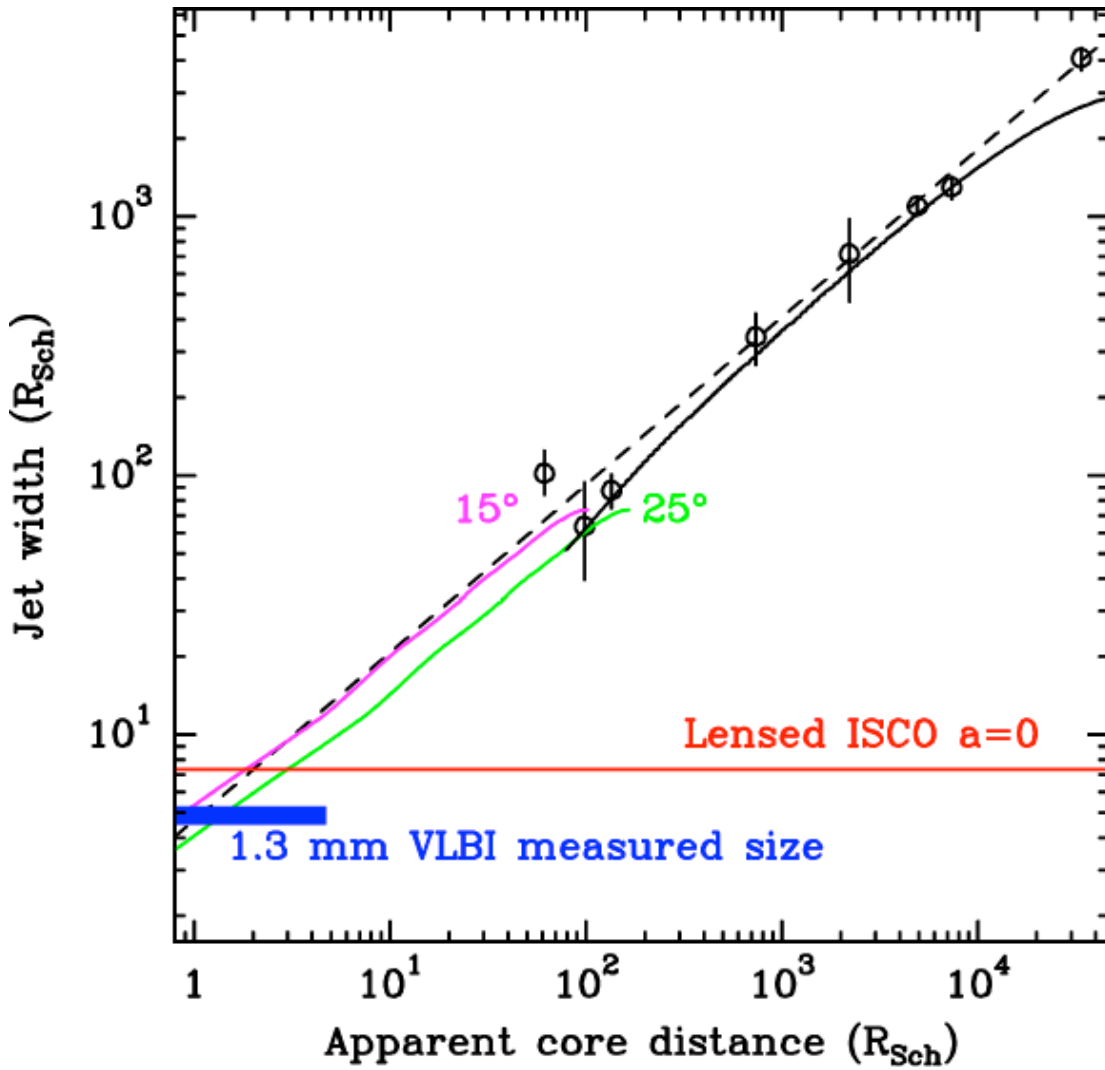


Fig. 2. Width profile of the M87 jet as a function of distance from the core. Measurements of jet opening angle from the literature (32) were converted to projected jet width, and fit with a power law (dashed black line) of the form $\theta \propto r^\beta$ where θ is jet width and r is separation from the core. The best fit $\theta \propto r^{0.69}$ indicates a parabola-like profile for the jet with collimation increasing at larger distances as expected from MHD theory, and is in agreement with recent detailed measurements of the M87 jet profile (18). The dark blue horizontal line indicates the size reported in this paper, with the thickness of the line corresponding to 3σ uncertainties. To estimate the position relative to the central black hole, we extrapolate the power law fit, which intersects the 1.3mm VLBI size at an apparent core distance of $\sim 1.25 R_{\text{SCH}}$. GRMHD models, tailored to simulate jet emission from the black hole out to distances of $\sim 100 R_{\text{SCH}}$, are shown as the solid red and green lines for jet axis angles to our line of sight of 15 and 25 degrees respectively (19). These close-in simulations also intersect the 1.3mm VLBI size between 1 and $2 R_{\text{SCH}}$ from the black hole. For comparison and illustration, jet width values derived from a separate GRMHD simulation of the larger scale M87 jet (20) are shown as a solid black line for distances larger than $\sim 100 R_{\text{SCH}}$. The red horizontal line indicates the apparent size of the Innermost Stable Circular Orbit (for a non-spinning black hole) when strong gravitational lensing effects near the black hole are properly accounted for (see SI for details).

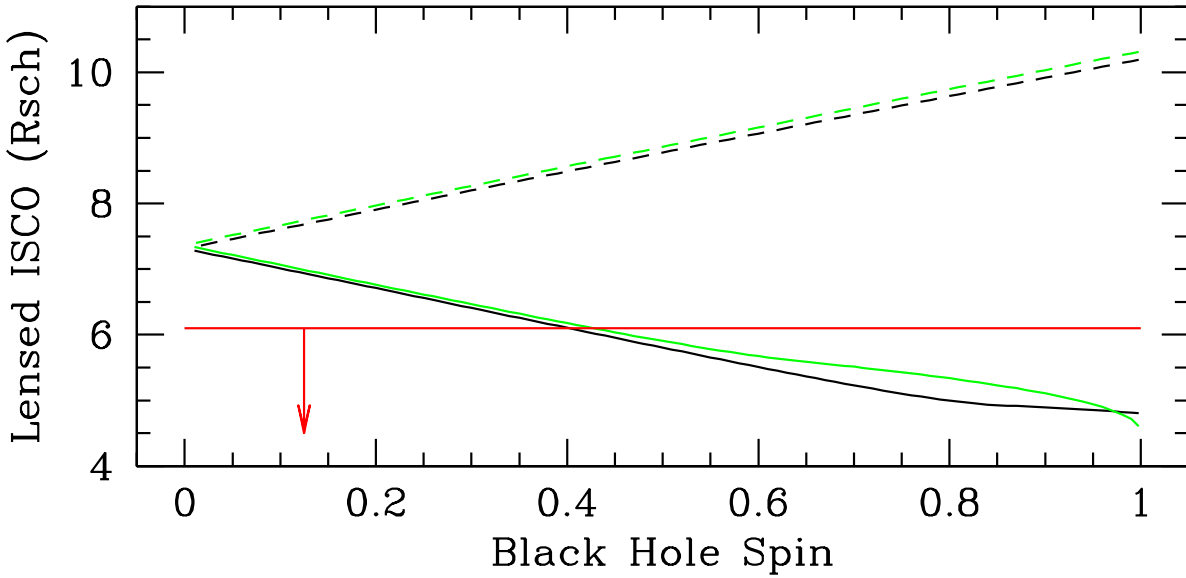


Fig. 3. Size of the Innermost Stable Circular Orbit of a black hole for arbitrary black hole spin. The apparent diameter of the ISCO due to the strong gravitational lensing near the black hole is computed using ray-tracing algorithms through Kerr space-time (33,34). Two scenarios are shown. The black curve is the apparent diameter of an opaque sphere whose radius coincides with the ISCO, and is viewed along the spin axis of the black hole. This distribution approximates a thick accretion disk, which is appropriate for M87. The green curve is the apparent diameter for a ring of emission at the ISCO as viewed in the orbital plane (analytic expressions given in SI). Solid lines show prograde ($a > 0$) orbits and dashed lines show retrograde ($a < 0$) orbits. The upper 3σ limit on the 1.3mm VLBI size derived in this work (shown as red line) intersects the lensed ISCO size for both cases at a spin of $a \sim 0.4$. Spins higher than this value are consistent with the jet base size derived here.

Supplementary Materials:

Figures S1-S4

Tables S1-S2

References (35-39)

Supplementary Materials:

Observations and Calibration

M87 was observed over the first half of the night on each of 2009 April 5-7, using an array consisting of the JCMT on Mauna Kea (J), the SMT in Arizona (S), and two dishes from the CARMA array in California (C and D). On the summit of Mauna Kea in Hawaii, the Submillimeter Array (SMA) housed the VLBI recording system and synthesized the Hydrogen Maser based VLBI frequency reference used at the JCMT. The observational setup and correlation for this observing campaign have been described in detail elsewhere (35). The baseline coverage of the observations over the three days is shown in Figure S1.

Once correlated using the Mark4 VLBI correlator at Haystack Observatory, data for each VLBI scan (typically 10 minutes) were segmented into smaller intervals corresponding to the coherence time of the atmosphere. This coherence time was typically between 3--20 seconds, and was measured independently for each scan. For each baseline, these segments were noise de-biased and incoherently averaged to remove any decorrelation due to atmospheric turbulence using a standard data reduction package developed at Haystack Observatory for high frequency VLBI data reduction (35-38). VLBI detections were determined through a 2-d search over interferometer delay and delay-rate using these incoherent averages.

To convert the processed data to units of correlated flux density, the VLBI correlation coefficient for each baseline was multiplied by the geometric mean of the System Equivalent Flux Density (SEFD) of both antennas. Measured in Janskys (Jy), the SEFD is a product of antenna gain (Jy/K) and the opacity corrected system temperature (T_{sys}). For all three sites, T_{sys} was measured just prior to each ~10 minute VLBI scan using a vane calibration technique that corrects for the atmosphere. For the JCMT and SMT, antenna gains were determined from observations of planets at several points during the multiple day campaign, and the gains were observed to be stable. Relative gains for the two CARMA dishes were estimated using observations taken by CARMA in interferometric array mode before each VLBI scan, and the gains were then set to a common flux scale using planet scans at the end of each night. The results of this a-priori calibration of the VLBI amplitudes are shown in Figure S2.

Large scale (~arcsecond) structure due to the relativistic jet in M87 causes beating in the amplitudes on the short baseline between the two CARMA antennas. The jet structure was imaged using CARMA array calibration data taken before each VLBI scan, and the resulting map is shown in Figure S3. The total flux density of M87 measured with the CARMA array was 1.9 Jy, and the value measured at the Submillimeter Array was 1.97 Jy. We have adopted the SMA value and adjusted the flux density level in the large scale M87 image accordingly.

After the a-priori calibration, there were clear differences between amplitudes on the CARMA-CARMA (CD) VLBI baseline and the amplitudes expected from the CARMA image (Figure S3). These differences may be due to imperfect determination of antenna SEFD or pointing errors. These same errors cause amplitude variation between baseline pairs to the two CARMA

dishes (e.g., SC and SD or JC and JD). Variations within each scan between the two observing bands are caused by instrumental differences in the signal paths at each antenna for each band.

These residual calibration errors and amplitude variation were corrected as described in previous work (35). After the gain-corrections are applied, the CD amplitudes track the model amplitudes (with signal to noise determined by averaging the high and low band CD detections together), and the SD and SC baseline amplitudes are averaged to a single value per VLBI scan (again with signal to noise determined by computing the weighted average). The effect of gain-correction on the JC, JD, and SJ baselines is minimal (<5%).

The short CD baseline is sensitive to emission on arcsecond scales, and variations of 10% in the amplitudes on this baseline are due to beating between the bright core and “knot A”, compact emission due to a shock in the jet 12 arcseconds downstream. The dropoff of ~ 1 Jy between the very short CD baseline and the SMT-CARMA baselines (SC and SD) is indicative of resolved jet structure on scales larger than $300 \mu\text{as}$. A similar dropoff is seen with 7 mm VLBI where arrays with more telescopes are able to map the extended emission in the jet on these scales (16).

Circular Gaussian Fits

Results of Gaussian fits on each day of observations are shown in Table S1. Data on the long baselines between the geographically separated sites (CARMA, JCMT, SMTO) were fitted using weighted least-squares to a circular Gaussian model parameterized by the Full Width Half Maximum (FWHM) and the total flux density. Contours of χ^2 were used to determine the uncertainty in each parameter (Table 1).

Lensed Size of the Innermost Stable Circular Orbit for Arbitrary Black Hole Spin

The radius of the Innermost Stable Circular Orbit (ISCO) for a black hole of arbitrary spin is given (in units of M) by (39)

$$R_{ISCO} = M \left(3 + Z_2 \mp [(3 - Z_1)(3 + Z_1 + 2Z_2)]^{1/2} \right) \quad (1)$$

$$Z_1 = 1 + \left[(1 - a^2 / M^2)^{1/3} \right] \left[(1 + a / M)^{1/3} + (1 - a / M)^{1/3} \right] \quad (2)$$

$$Z_2 = \left(3a^2 / M^2 + Z_1^2 \right)^{1/2} \quad (3)$$

The upper sign in Eq. 1 is used for prograde orbits and the lower sign used for retrograde orbits.

The last photon orbit in the equatorial plane for a black hole with arbitrary spin is given by

$$r_{\pm\gamma} = 2M \left\{ 1 + \cos \left(\frac{2}{3} \cos^{-1} (\mp a / M) \right) \right\} \quad (4)$$

In the equatorial plane, the apparent radius of the ISCO for an observer at infinity is given by (26)

$$R_a = (b_+ - b_-) / 2 \quad (5)$$

where

$$b_{\pm} = \pm \begin{cases} R \left(\frac{R \sqrt{R^2 - 2MR + a^2} \mp 2aM}{R^2 - 2MR} \right) & \text{if } R > r_{\pm\gamma} \\ r_{\pm\gamma} \left(\frac{r_{\pm\gamma} \sqrt{r_{\pm\gamma}^2 - 2Mr_{\pm\gamma} + a^2} \mp 2aM}{r_{\pm\gamma}^2 - 2Mr_{\pm\gamma}} \right) & \text{if } R < r_{\pm\gamma} \end{cases} \quad (6)$$

Figure 3 in the main report shows the intrinsic ISCO size and the apparent ISCO size as a function of black hole spin both in the equatorial plane (equation 6) and looking down the axis of rotation of the black hole (through ray-tracing simulations).

Calibrated 1.3~mm VLBI Data

Table 2 contains all of the VLBI data used for the size analysis in this work. For brevity, only the first ten lines are shown here to describe the formatting of the table.

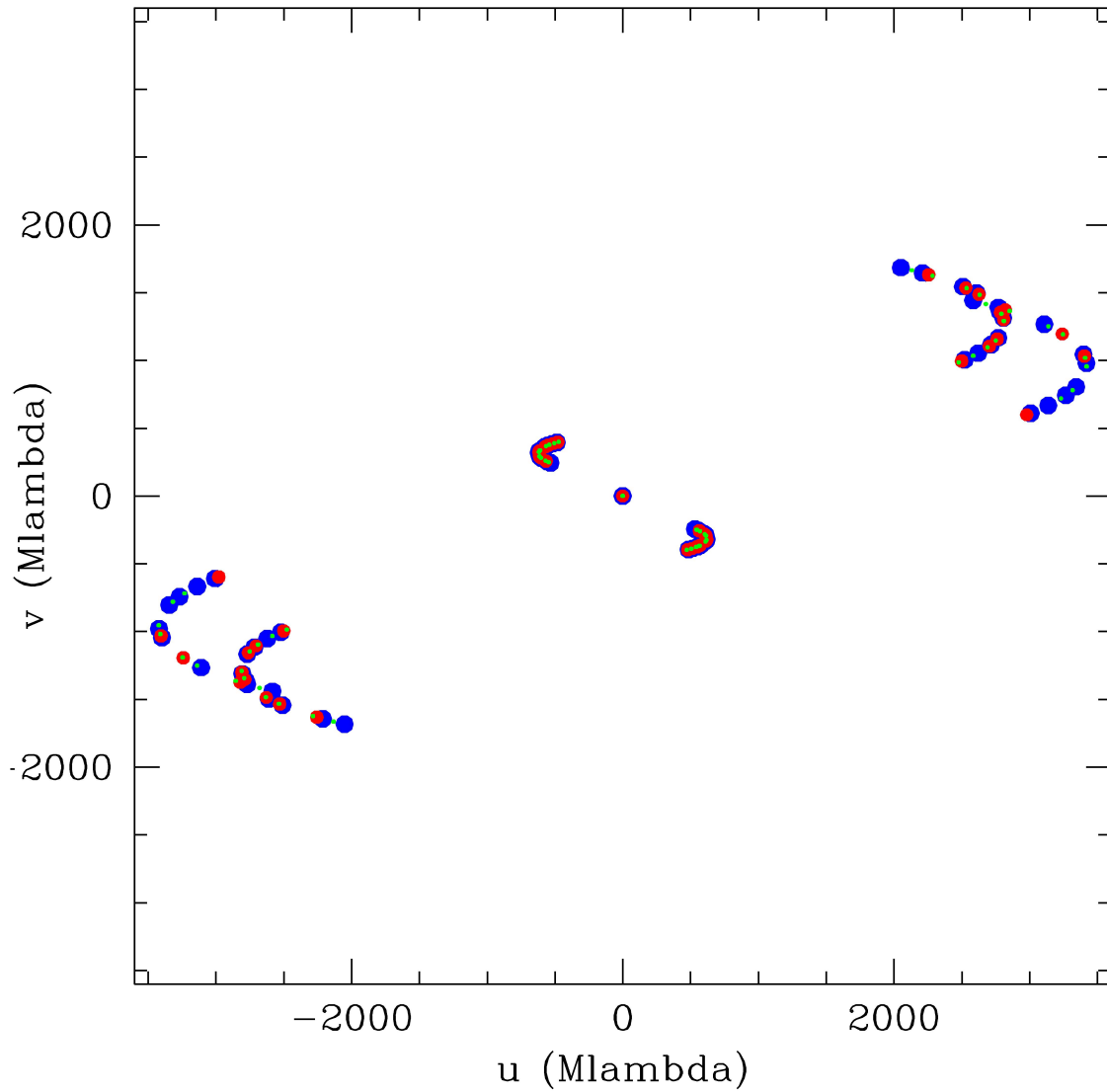


Fig S1. Baseline spacings for 1.3mm VLBI observations of M87 during nights of 2009 April 5, 6, and 7 (green, red, and blue points, respectively). The plot only shows (u,v) points for which M87 detections were obtained (incoherent SNR > 3.8).

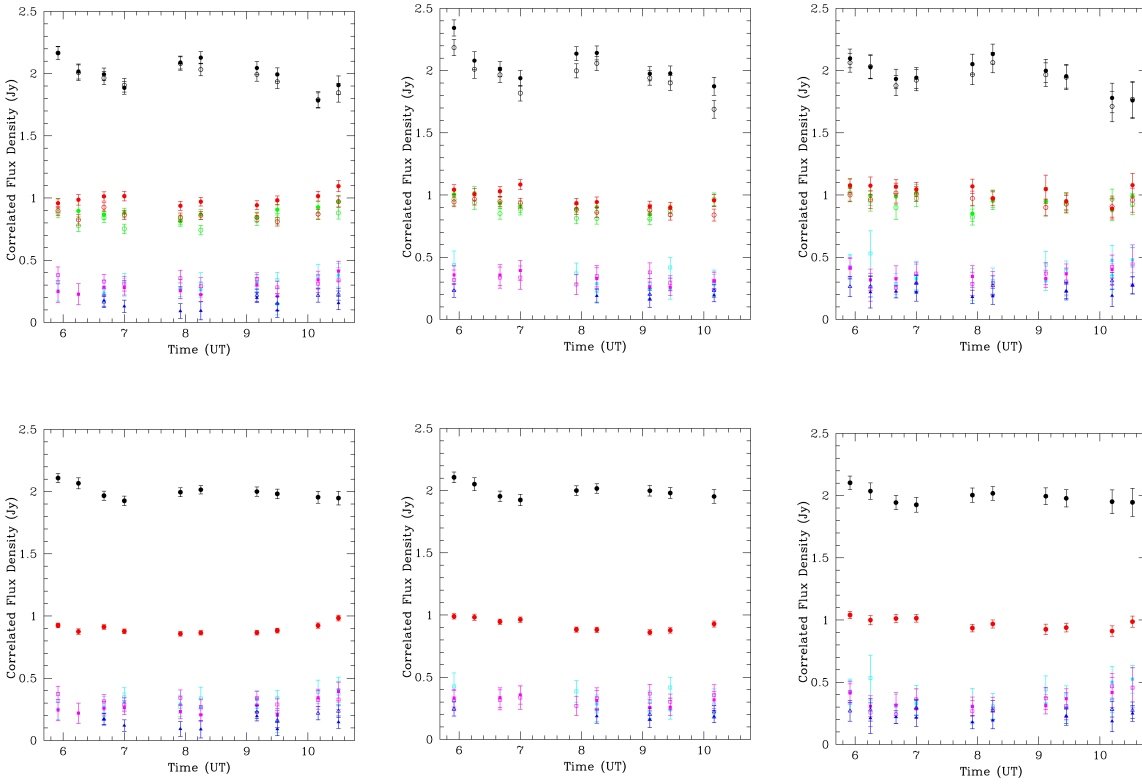


Fig S2. {Top}: A-priori calibrated visibility amplitudes of M87 as a function of time. Open symbols are data from the low band, and filled symbols from the high band. Black points are amplitudes on the short baseline between the two CARMA dishes. Red and green points are the SMT-CARMA baselines. Magenta and cyan points show the JCMT-CARMA baselines, and dark blue points are used for the SMT-JCMT baseline. Error bars show the *random* error only. *Bottom*: The same data after gain correction using the large scale model for M87 determined from data taken by the CARMA array. Gain-corrected SC and SD data are equal by definition.

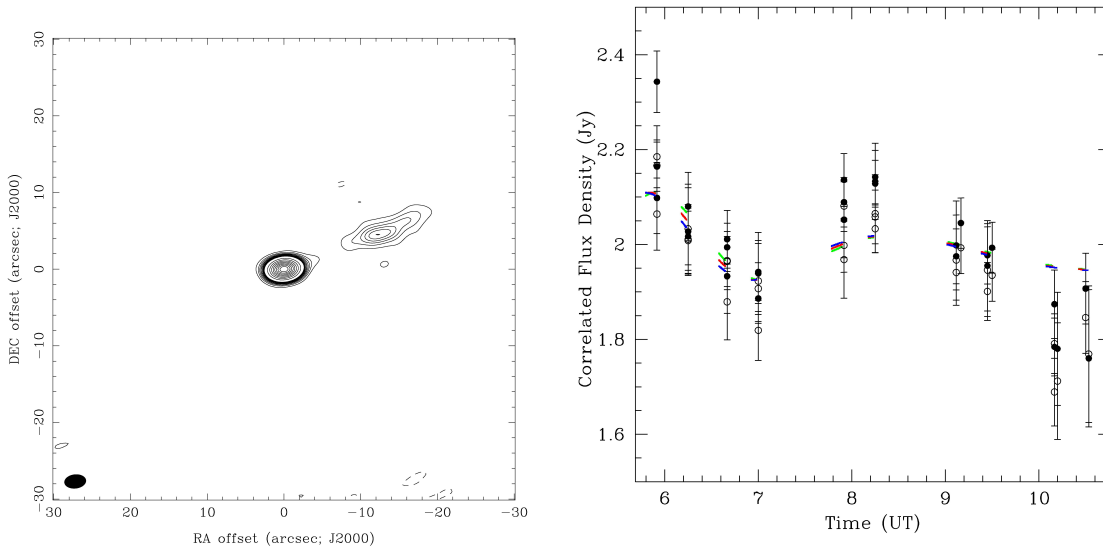


Fig S3. {Left}: An image of M87 on arcsecond scales made using data taken by the CARMA array during the 1.3mm VLBI observations. The well-known ‘knot A’ feature in the jet ~ 12 arcsec from the core is clearly detected. Contour levels (in units of 0.019 Jy/Beam): -3, -2, -1, 1, 2, 3, 4, 5, 6, 7, 8, 9, 10, 20, 30, 40, 50, 60, 70, 80, 90. {Right}: Plot of the VLBI visibility amplitudes after a-priori calibration, along with colored points showing visibilities at contemporaneous times derived from the source model. Corrections to the calibration of both CARMA antennas are derived by forcing the VLBI amplitudes to match the model. Green, red, and blue model points correspond to days 095, 096, and 097 respectively. Errors in the a-priori calibrated data are random errors added in quadrature to 5% errors due to a-priori calibration uncertainty.

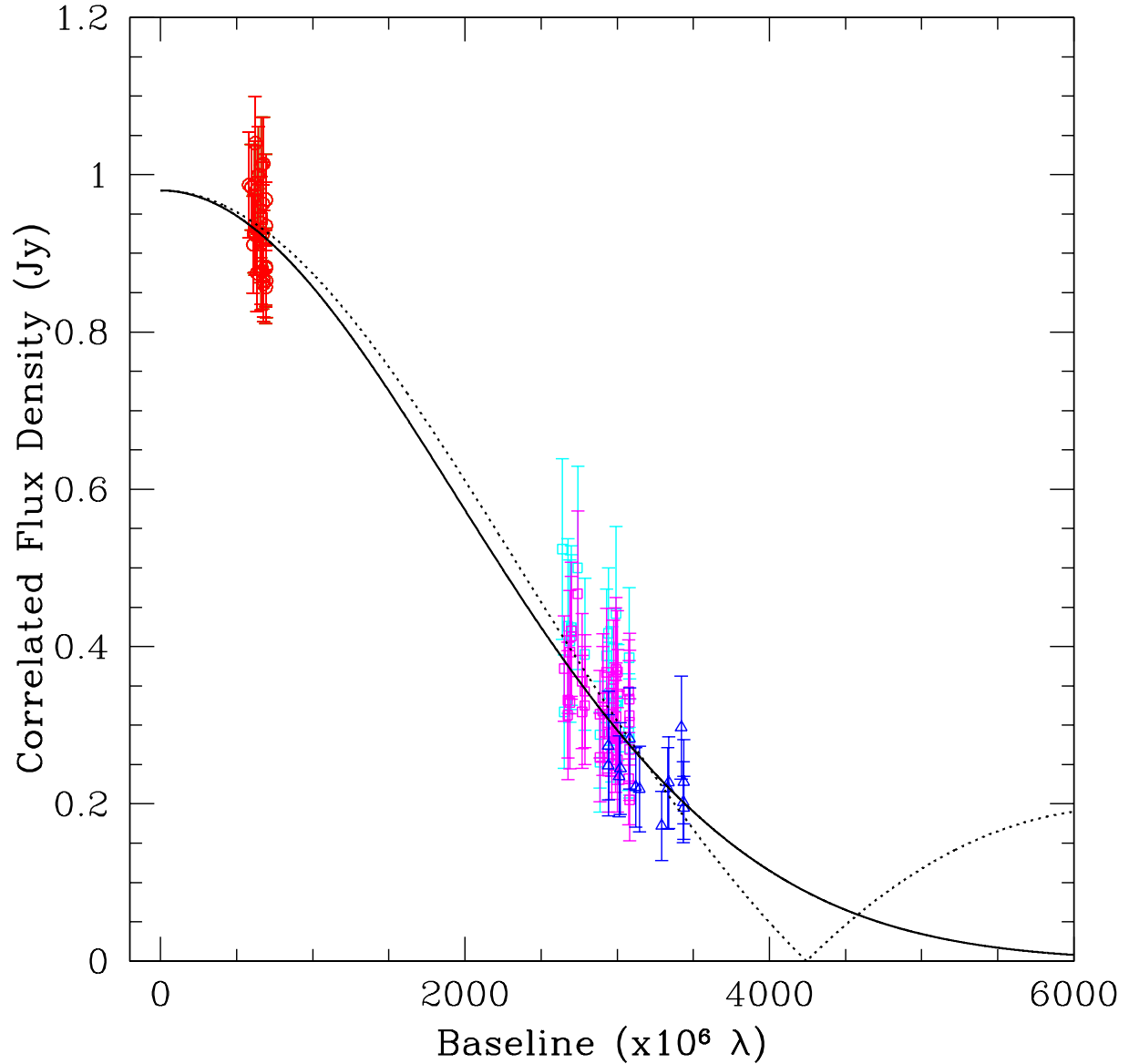


Fig S4. Circular Gaussian and hybrid model fits to 1.3mm VLBI data from three days of observations. The weighted least squares best-fit circular Gaussian model has a total flux density of 0.98 Jy and a FWHM size of 40.0 micro arcseconds (shown as a solid line). The hybrid model (dotted line) combines a circular Gaussian of the same size with a thin ring of diameter 40.0 micro arcseconds, which represents the expected ‘shadow’ feature due to illumination of the central supermassive black hole from behind by a counter-jet in M87. In the hybrid model, the Gaussian and ring components each contribute one-half the flux density. On VLBI baselines shorter than the null spacing, the interferometric phase will be zero, but on baselines beyond the null spacing, the phase will rotate by 180 degrees. This characteristic, along with the increasing flux density exhibited by the hybrid model on long baselines, will enable future VLBI arrays to distinguish between these two models. The data points follow the color scheme in Figure S2. Errors on the data include 5% calibration uncertainty added in quadrature with the intrinsic random errors.

Table S1. Circular Gaussian Fits to M87. Errors are 3σ

Day Number	Compact Flux Density (Jy)	Size FWHM (μas)
95	$0.95^{+0.06}_{-0.06}$	$40.3^{+2.5}_{-2.6}$
96	$0.97^{+0.07}_{-0.06}$	$39.8^{+3.8}_{-3.3}$
97	$1.03^{+0.05}_{-0.054}$	$39.1^{+3.5}_{-3.4}$
all days	$0.98^{+0.04}_{-0.04}$	$40.0^{+1.8}_{-1.8}$

Table S2. Gain-Corrected Detections of M87

Day	Time (UT)	Baseline	Band	u ($k\lambda$)	v ($k\lambda$)	Flux Density (Jy)	σ (Jy)
95	05:55	CD	low	1	-40	2.11	0.11
95	05:55	JC	low	2463469	980845	0.32	0.07
95	05:55	JD	low	2463470	980805	0.37	0.07
95	05:55	SC	low	-469518	396541	0.93	0.05
95	06:15	CD	low	3	-40	2.07	0.11
95	06:15	SC	low	-502735	387407	0.88	0.05
95	06:40	CD	low	7	-40	1.97	0.10
95	06:40	JC	low	2674795	1089740	0.29	0.07
95	06:40	JD	low	2674802	1089700	0.31	0.06
95	06:40	SC	low	-538819	375171	0.91	0.05

Note. — 1.3mm VLBI detections of M87 in April 2009. Scans are referred to by day of year, UT start time, baseline, and observing band. The projections of the baseline length east and north in the direction of M87 as measured in units of thousands of wavelengths are indicated as u and v . The error on the detected flux density includes a 5% systematic component added in quadrature to the random error.

References: Additional references should be cited here and included in the main reference list.

35. V. L. Fish, *et al.*, 1.3 mm wavelength VLBI of Sagittarius A*: detection of time-variable emission on event horizon scales, *Astrophys. J.* **727**, L36 (2011).
36. S. S. Doeleman, *et al.*, Structure of Sagittarius A* at 86 GHz using VLBI closure quantities, *Astron. J.* **121**, 2610 (2001).
37. S. S. Doeleman, *et al.*, Event-horizon-scale structure in the supermassive black hole candidate at the Galactic Centre, *Nature* **455**, 78 (2008).

38. A. E. E. Rogers, S. S. Doeleman, J. M. Moran, Fringe detection methods for very long baseline arrays, *Astron. J.* **109**, 1391 (1995).
39. J. M. Bardeen, W. H. Press, S. A. Teukolsky, Rotating black holes: locally nonrotating frames, energy extraction, and scalar synchrotron radiation, *Astrophys. J.* **178**, 347 (1972).